An External Force Sensing System for Minimally Invasive Robotic Surgery

Giuseppe Andrea Fontanelli, Luca Rosario Buonocore, Fanny Ficuciello, *Senior Member, IEEE*, Luigi Villani, *Senior Member, IEEE*, and Bruno Siciliano, *Fellow, IEEE*

***Abstract*—Minimally invasive robotic surgery (MIRS) has revolutionized surgical procedures. However, compared to classic laparoscopy, the surgeon must rely only on visual perception because of the lack of force feedback. In this article, a new noninvasive force feedback system is proposed and evaluated. Extending the work by Fontanelli (2017), where preliminary results were presented, a solution based on a novel force sensor placed in the terminal part of the trocar is shown in detail. With respect to the state of the art, our system allows measuring the interaction forces between the surgical instrument and the environment inside the patient's body without any changes to the instrument structure and with full adaptability to different robotic platforms and surgical tools. Using a commercial force-torque sensor as ground truth, the static and dynamic characterization of the sensor is provided together with an extensive experimental validation. Finally, a simple and intuitive application of the proposed sensing system in a realistic surgical scenario is presented.**

***Index Terms*—Force estimation, force sensor, minimally invasive surgery, robotic surgery.**

I. Introduction

THE main advantages for which robotics is taking a key role in surgery and, in particular, in laparoscopic surgery are minimized postoperative pain, speed up of the recovery time, increased comfort for the surgeon, improved surgical performance, and reduced hemorrhaging and risk of infections. However, the lack of force feedback in surgical robots can potentially lead to tissue damage and bad execution of particular tasks, such as suturing and intraoperative decisions, that would require feeling the tissue deformation. Most of the currently available robotic surgery systems do not have haptic feedback capability. Surgeons do not have the possibility to feel the suture thread tensile force or the pressure applied to organs and tissues. Hence, during some surgical procedures, thread breakage or tissue damage may occur, especially for less experienced surgeons. Another problem is the impossibility to identify undesired interactions between the instruments and the tissues outside the viewing area. Consequently, experience and ability of the surgeon make the difference. Indeed, studies on this topic [2] show that haptic feedback could reduce unintentional injuries and learning time for novices. Moreover, force feedback would allow implementing advanced control algorithms (impedance/force control, adaptive virtual fixtures [3], bilateral telemanipulation control) to enhance the effectiveness and dependability of surgical robots [4], [5].

Several works on the development of force sensing to measure the interaction between surgical instruments and the patient body are available in the literature. Some of them investigate the possibility to provide force measurement without making changes to the robot, e.g., in [6], using only visual information or, as in [7] and [8], using the control torques and the dynamic model of the robot.

Many prototypes of sensorized surgical instruments have been developed by integrating force sensors in the instrument shaft or wrist, or even in the gripper fingers and clamp faces. In [9], strain gauges are glued on the instrument shaft to measure force and torque on a laparoscopic instrument. In [10], a six-axis force sensor using Bragg reticula is presented, while in [11]–[13], fiber-optic technology is used to build miniaturized and robust force sensors for different surgical applications. As reported in these works, the fiber-optic technology has many advantages, including the high miniaturization capability and the immunity to electromagnetic interference (EMI) noise. Optical or thin-film organic solutions, such as those presented, respectively, in [14] and [15], to develop a sensitive skin could be adapted for sensing the forces directly on the surgical gripper or on the instrument shaft. Moreover, promising studies on miniaturized force sensors adopt micro-elelctro-mechanical systems (MEMS) technology [16] as well as piezoelectric [17] and capacitive effects [18], [19]; the sensing devices are placed inside the instrument gripper or in the wrist.

The common feature of the abovementioned works is that they require the modification of the instrument structure to host the force sensor. This entails higher costs, problems related to sterilization, increased likelihood of instrument breakage, the need of miniaturizing complex structures able to withstand high stresses, and problems related to the tendon-driven mechanisms of the instruments. Moreover, the instruments may be used for a

Manuscript received June 22, 2018; revised February 13, 2019 and December 13, 2019; accepted February 3, 2020. Date of publication March 9, 2020; date of current version June 15, 2020. Recommended by Technical Editor F. Janabi-Sharifi. This work was supported in part by the POR FESR 2014–2020 Italian National Programme under BARTOLO Project CUP B41C17000090007 and in part by the PNR 2015–2020 Italian National Programme under PROSCAN Project CUP UNINA: E26C18000170005. *(Corresponding author: Giuseppe Andrea Fontanelli.)*

The authors are with the Department of Electrical Engineering and Information Technology and the Interdepartmental Center for Advances in Robotic Surgery, University of Naples Federico II, 80125 Napoli, Italy (e-mail: g.a.fontanelli@gmail.com; luca.buonocore@gmail.com; fanny.ficuciello@unina.it; lvillani@unina.it; bruno.siciliano@unina.it).

Color versions of one or more of the figures in this article are available online at http://ieeexplore.ieee.org.

Digital Object Identifier 10.1109/TMECH.2020.2979027

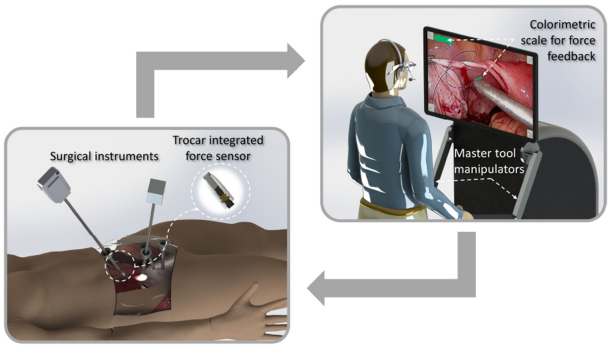

Fig. 1. Sketch describing the framework of the proposed force sensing system.

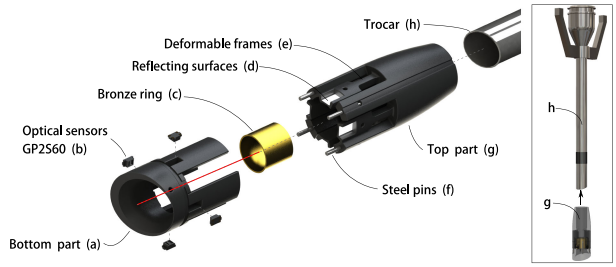

Fig. 2. Exploded view of the force sensor CAD model. The assembly of the sensor on the trocar by interference is illustrated on the right.

limited number of interventions and thus, the cost of the sensor represents an additional cost for each surgical procedure.

In this article, a novel solution for sensing the interaction force between the robot tool and the patient body is proposed and evaluated. The sensing device is capable of measuring the forces in the orthogonal plane to the shaft of the surgical instrument. The idea is to place the sensor in the trocar, with minimal modification of its structure and without modifying the surgical instrument (see Fig. 1). This allows reducing costs and saving time. Moreover, this solution can be fully adapted to different robotic platforms and surgical tools [20].

The price to pay is that the axial force component, i.e., the force acting along the axis of the instrument shaft, cannot be directly measured. This problem is overcome here by adopting the residual-based estimation method of [21] to estimate only the axial force component. This requires the knowledge of a reduced set of dynamic parameters of the robot and of the instrument. An alternative but more expensive solution which allows the direct measurement of all the three force components, based on a sensorized tool adapter for the da Vinci system, can be found in [22].

In this article, the accuracy of the proposed trocar sensor is evaluated experimentally, by using the da Vinci Research Kit (dVRK) [23], the research version of the da Vinci system, as a surgical robotic platform and a first prototype of the sensor.

Besides testing the capability of the sensor to measure the external forces, this article presents a simple example of using the force information to improve the surgeon perception, also in the absence of the measurement of the axial force component. To this purpose, the main approaches proposed in the literature are: 1) kinesthetic feedback, in which the force estimated on the slave side is applied on the master robot, e.g., [24]; 2) cutaneous force feedback, which allows perceiving the force via sensory substitution using wearable devices, e.g., [25]; and 3) visual force feedback, in which the force information is retrieved via sensory substitution in augmented reality [26]. The third approach is used here to test our sensing device.

The rest of this article is organized as follows. In Section II, the sensor operating principle is presented. Section III describes the static and dynamic characterization of the sensor and presents the residual-based method to estimate the external forces. Section IV reports the experimental validation. An application where the sensor is used to provide visual force feedback to the surgeon is presented in Section V. Some issues resulting from the evaluation of the sensor prototype are discussed in Section VI. Section VII concludes this article.

II. Sensor Operating Principle

The innovation of the solution proposed in this article concerns the sensing element that is allocated at the end-tip of the trocar. Fig. 1 shows a sketch of the proposed idea with a zoomed view of the trocar where the sensor is placed.

The sensor is composed of a bronze ring that has an inner diameter lower than the inner diameter of the trocar; the bronze ring is glued to a deformable structure (see Fig. 2). The inner diameter of the bronze ring is still greater than the diameter of the instrument shaft. The interaction force between the instrument end-effector and the patient body produces a displacement of the bronze ring, pushed by the instrument shaft, with respect to the trocar axis, which causes the deformation of the elastic frames that compose the sensor. This deformation, which depends on the elasticity of the deformable elements and is measured using four proximity optical sensors mounted in the appropriate way, is proportional to the force applied by the shaft to the ring.

More specifically, consider a sensor reference frame O_S-$x_S y_S z_S$ attached to the sensor, with the axes x_S and y_S lying on a plane orthogonal to the trocar axis. The deformation of the elastic frames is proportional to the forces applied along the axes x_S and y_S to the ring.

This solution has a number of advantages, which includes the following:

1) the trocar sensor is cheap and can be used with different surgical instruments, which can be replaced easily during the surgical procedure and no modification of the robot structure is required;
2) the forces measured by the trocar sensor are not influenced by the tendon forces, as it happens for the sensors located in the instrument shaft;
3) compared to the solutions with sensors located at the end-tip of the instrument, the connection cables and the data acquisition system of the trocar sensor are fixed and far away from the surgical site.

Of course, the proposed solution requires that the minimally invasive robotic surgery (MIRS) instruments have a constant diameter and is particularly useful in the case that different

instruments have the same diameter. These limitations are not critical considering that they are verified in the da Vinci surgical robotic system.

A. Mechanical Design

The exploded view of the computer-aided design (CAD) model of the trocar sensor is shown in Fig. 2. The sensor is composed of three main parts. The top part (g) is attached at the trocar end-tip by interference in order to simplify the assembly (see Fig. 2 right). It is composed of four deformable frames designed with four digs holding flat reflective surfaces; the surgical instrument slides inside a bronze ring (c) that is glued on the four deformable frames. The bronze ring ensures a homogeneous deformation of the four deformable frames when a force is applied by the instrument shaft; moreover, it allows to reduce the sliding friction and to reinforce the overall structure. In order to measure the deformation, four optical sensors are fixed to the bottom part of the sensor (a) in correspondence with the reflective surfaces. Four trays have been suitably designed to lock the optical sensors in the required position and, more importantly, at a precise distance from the reflective surface.

In this first prototype, the parts have been produced in plastic using a three-dimensional (3-D) printing technology based on the PolyJet process. This technology was chosen due to the high precision (minimum layer thickness of about 28 μm and minimum resolution of about 0.1 mm) and quick fabrication time, without requiring cleaning or postprint treatments. However, it is not suitable for a real working version of the sensor, because the mechanical properties of the printed material are not stable and change with time. The minimum feature size in the design is 0.2 mm.

The mechanical design was supported by the use of a finite-element model (FEM) optimization procedure to compute the optimal dimensions of the deformable frames according to the following specifications:

1) the force along x_S and y_S axes set in the range $[-20, 20]$ N;
2) the maximum von Mises stress (safety factor) settled as two times the value of the material yield stress, which is in the range $[50, 65]$ MPa;
3) minimum size of the overall structure, especially the diameter, compatible with the constraints of the printer.

According to [27] and [28], the forces applied during suturing are in the range $[-10, 10]$ N. Indeed, during needle insertion, the average force is about 3 N while, during knot tying, the force can reach 10 N.

The prototype was verified using FEM analysis to validate the expectations of the project prerequirements. The behavior of the trocar sensor was simulated considering the point O on the top of the tool as stuck (see Fig. 3 top). In the same way, the end-tip of the trocar can be considered as a fixed point since it constitutes a constraint for the motion of the tool shaft, except for the sliding motion. In this configuration, the tool is placed with respect to the trocar in such a way that the distance of the end effector frame from point O is two times the distance of the sensor frame from the same point. Hence, when a force of 10 N is applied to the instrument end-effector frame O_E-$x_E y_E z_E$ along the x_E axis, due to the lever effect, a 20-N force results on the sensor frame along the x_S axis. Notice that only static conditions are considered in this analysis. The von Mises stress and the displacements of the four reflective surfaces are shown in Fig. 3 (bottom).

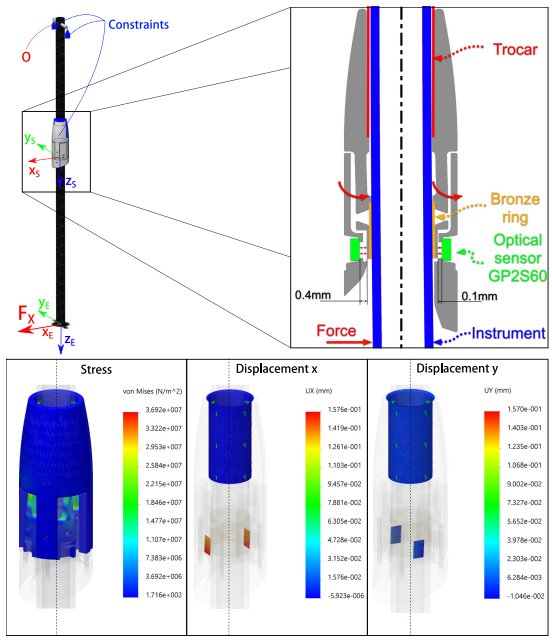

Fig. 3. FEM analysis results. Top: Schematic of the instrument with the relevant reference frames and zoomed section of the trocar sensor. Bottom: von Mises stress and displacements along x_S and y_S axes in the case of a 10-N force applied to the tip along the x_E axis.

It can be seen that the von Mises stress on the deformable structure is about half of the yield stress value, which for the used material is around $6.5e^7$ N/m^2. Moreover, a force applied along the x_S-axis causes a displacement of the reflecting surfaces perpendicular to the x_S-axis (in orange) while the other two surfaces (in blue) do not move. Therefore, the deformations due to forces along the x_S and y_S axes are decoupled as desired.

The zoomed section of the sensor represented in Fig. 3 (top) shows the eccentricity between the instrument shaft and the fixed trocar caused by the force applied to the instrument tip. In detail, it is possible to observe how the interaction force between the instrument and the environment causes a displacement of the instrument shaft that collides with the bronze ring of the trocar sensor glued to the four deformable frames. The displacement of the frames orthogonal to the direction of the force is quoted in the zoomed section for an applied force of 20 N in the sensor frame. Notice that the contact point of the instrument shaft with the bronze ring may be uncertain due to the finite length of the bronze ring and may cause an error on the force measurement. This error could be avoided or reduced by suitably shaping the internal surface of the bronze ring so as to have a single contact point.

B. Optical Sensors and Electronics

In the tested prototype, the measurement of the deformation of the frames is obtained using four $GP2S60$ proximity optical

sensors. We have chosen this technology for the following reasons.

1) Compared to other solutions, the sensor is not expensive.
2) The sensor signal can be read with a very simple conditioning circuit.
3) With respect to fiber Bragg-based sensors, our solution is considerably cheaper and the measurement is not influenced by fiber bendings.
4) With respect to solutions based on the strain estimation of a deformable structure (strain gauge, fiber Bragg), the proposed design is less influenced by forces applied on the structure in the direction orthogonal to the measured force.

Moreover, to reduce the light interference between all the sensors and the environment, the sensors are positioned on suitably designed trays painted in black. To improve the sensitivity of the device, the four proximity sensors are located at 90° one from the other, and thus, they are in couple one in front of the other. Therefore, for a given displacement of the sensitive structure, one sensor detects a positive displacement while the opposite one detects a negative displacement. These differential readings allow doubling the gain of the device.

Each optical sensor is equipped with an IR source and a photodiode detector capable of measuring the amount of reflected light, which is related to the distance of the sensor from the reflective surface placed in front of it. This system is affected by light interference and cross-talk disturbance. In our prototype, the four trays are designed to reduce these effects and all the external parts of the trocar sensor are painted in black, except for the reflective surfaces that are painted in white. Moreover, the overall structure of the sensitive device was designed to reduce the external light disturbances.

The use of proximity optical sensors instead of other sensing solutions has the advantage that the electronics needed to acquire the signals is very simple. Namely, only a polarization circuit and an analog-to-digital converter (ADC) are required.

In the presented prototype, the ADS1015 ADC was selected, since it is equipped with a four-channel converter which offers the possibility to read in differential mode and to amplify the input signal with an internal amplifier. The amplification factor G was set to the maximum value to maximize the resolution in the measurement range. The maximum frame rate of the ADC is 1.5 kHz for the differential acquisition mode, with a 12-b resolution. Finally, the ADC is provided with a serial bus I2C which allows using only four connection wires to communicate with the microcontroller.

The microcontroller LPC1768, which is an mbed platform,[1] was used for signal processing. This device performs a numerical prefiltering with a sampling frequency of 1kHz.

Moreover, Fig. 4(a) reports the relating polarization circuit, where $R_1 = 330\ \Omega$, $R_2 = 15\ \text{k}\Omega$, $v_{cc} = 5$ V. Moreover, Fig. 4(b) shows the characteristic curve representing the relative collector current with respect to the distance between the sensor and the reflecting surface. This current value is reported as a percentage since it is a function of the device polarization

[1] [Online]. Available: https://developer.mbed.org/platforms

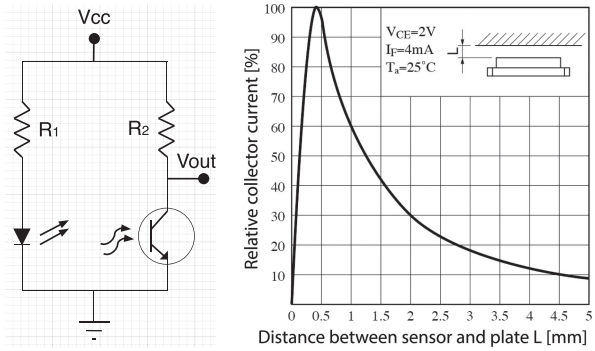

Fig. 4. (a) Polarization circuit and (b) characteristic curve of the GP2S60 optical sensor.

condition. Therefore, it depends on the maximum current $i_{C\max}$ and on the collector dark current i_{CEO} that flows in the device in the absence of light

$$i_{C\%} = \frac{i_C - i_{\text{CEO}}}{i_{C\max}}. \tag{1}$$

The sensor is used in the first part of the characteristic curve, i.e., in the region where the distance belongs to the interval $[0, 0.4]$ mm with almost linear characteristic and high gain. Let G_I be the gain in this linear region between the displacement of the sensor δ_x and the current $i_{C\%}$. By taking into account (1), the following relationship between the kth output sensor voltage $v_{\text{out},k}$ and the kth displacement $\delta_{x,k}$ can be found

$$\begin{aligned} v_{\text{out},k} &= v_{cc} - R_2 i_{C,k} = v_{cc} - R_2 i_{C\%,k} i_{C\max} + R_2 i_{\text{CEO}} \\ &= v_{cc} - R_2 G_I i_{C\max} \delta_{x,k} + R_2 i_{\text{CEO}}. \end{aligned} \tag{2}$$

In our design, the output voltage from the ADC, with gain G, is the difference between the output voltage of two opposite sensors. Assuming the same parameters $V_{cc}, R_2, I_{C\max}, G_I, I_{\text{CEO}}$ for each sensor, the output voltage for each couple is

$$v_s = G(v_{\text{out},2} - v_{\text{out},2}) = G G_I R_2 i_{C\max}(\delta_{x,2} - \delta_{x,2}). \tag{3}$$

Moreover, assuming $\delta_{x,1} = -\delta_{x,2} = \delta_x$, it is

$$\delta_x = \frac{1}{2 G G_I R_2 i_{C\max}} v_S = Q v_S. \tag{4}$$

Finally, if K is the stiffness coefficient modeling the elastic behavior of the deformable structure of the sensor, the external force can be computed as

$$f_S = K \delta_x = K Q v_S. \tag{5}$$

Therefore, the sensor calibration matrix $\boldsymbol{W}$ describing the relationship between the output voltage vector $\boldsymbol{v}_S \in \mathbb{R}^2$ and the vector $\boldsymbol{f}_S \in \mathbb{R}^2$ of the forces applied to the sensor can be defined as

$$\boldsymbol{W} = \begin{bmatrix} K_{11}Q & K_{12}Q \\ K_{21}Q & K_{22}Q \end{bmatrix}. \tag{6}$$

Two off-diagonal terms $K_{12}Q$ and $K_{21}Q$ have been introduced in the calibration matrix (6) to capture the nonperfect symmetry of the sensor and the residual cross-talk effects.

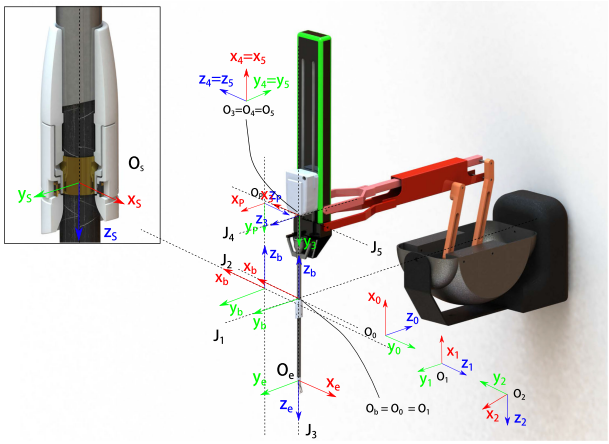

Fig. 5. da Vinci PSM robotic arm with the force sensor placed at the end of the trocar—kinematic frames description.

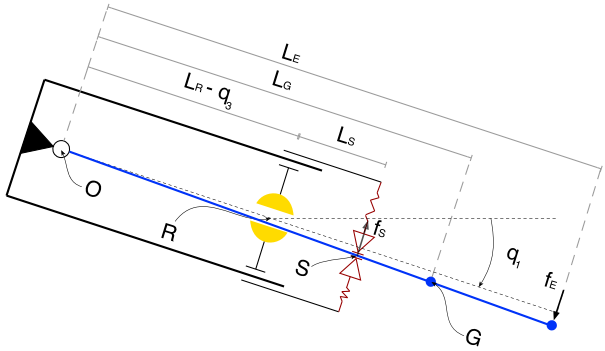

Fig. 6. Single-axis sensor operating principle. The points G, S, O, R are, respectively, the center of mass of the instrument shaft, the contact point between the instrument shaft and the sensor (bronze ring), the attaching point between the instrument shaft and the instrument box, and the RCM.

A software calibration procedure was implemented to compensate the residual bias due to the nonnegligible differences between the parameters of each sensor and their asymmetry.

III. Modeling and Calibration

The force $\boldsymbol{f}_S$ measured by the trocar sensor is influenced by the external force acting on the instrument shaft, but also by gravity and inertial forces due to the instrument motion.

Fig. 5 shows the sensing system mounted on the patient side manipulator (PSM) of a da Vinci surgical robot.

The PSM is a 7-DOF actuated arm, which moves the attached instrument with respect to a remote center of motion (RCM), i.e., a mechanically fixed point that is invariant with respect to the configuration of the PSM joints. The position of the instrument tip depends only on the first three joint variables, corresponding to revolute (R) and prismatic (P) joints in an RRP sequence. The corresponding joint axes are shown in Fig. 5, where they are denoted as J_i, $i = 1, 2, 3$. The last four joints allow the opening/closure and reorientation of the gripper mounted on the tip [29]. A counterweight, not represented in the figure, is used to balance the weight of the mass which translates with respect to the RCM.

The sensor is mounted on the terminal part of the trocar, in proximity of the RCM of the robot, which is located at the intersection of axes J_1 and J_2. Fig. 6 represents a planar view of the system, where the RCM is at point R in the center of the two yellow semicircles. In this figure, the shaft of the instrument (blue segment) is linked to point O, which corresponds to the intersection of axes J_4 and J_5 of Fig. 5, and can translate with respect to the RCM along axis J_3. The rotational motion of the shaft about the axes J_1 and J_2 is described by joint variables q_1 and q_2, while the translational motion along axis J_3 is described by q_3. The joints J_1, J_2, and J_3 are actuated by the motors of the PSM, and the corresponding joint variables are collected in the vector $\boldsymbol{q} = [q_1, q_2, q_3]^T$.

It is assumed that the external force $\boldsymbol{f}_E \in \mathbb{R}^3$ is applied to the end point of the shaft. The sensing element is placed on point S of Fig. 6, at a distance L_S from the RCM R. The sensor measures the displacement of the shaft with respect to its rest position under the action of the external force, gravity, and inertial forces, and $\boldsymbol{f}_S \in \mathbb{R}^2$ is the reaction force of the deformable part of the sensing element. To model this displacement, we assume that the shaft (a carbon fiber tube) is rigid and can rotate with respect to the pivot point O about the orthogonal axes J_4 and J_5 of Fig. 5, modeled as passive revolute joints. The corresponding joint variables are collected in the vector $\boldsymbol{q}_S = [q_4, q_5]^T$.

In static conditions and in the absence of gravity, the relationship between the force $\boldsymbol{f}_S$ applied to the sensor and the external force $\boldsymbol{f}_E$ depends only on the distance of the end point from point S as explained in Section III-A. This relationship is used in Section III-B for sensor calibration and in Section III-C for sensor characterization. In dynamic conditions, the weight and inertia of the instrument shaft must be suitably taken into account to estimate the external forces from sensor readings, as illustrated in Section III-D.

A. Static Modeling

In static conditions and in the absence of gravity, assuming that the shaft (a carbon fiber tube) is rigid and can only rotate about the axes J_4 and J_5, the relationship between $\boldsymbol{f}_S$ and $\boldsymbol{f}_E$ can be simply obtained from the static equilibrium of the corresponding torques about O as follows:

$$\boldsymbol{J}_E^T \boldsymbol{f}_E = \boldsymbol{J}_S^T(\boldsymbol{q}) \boldsymbol{f}_S \rightarrow \boldsymbol{f}_E = (\boldsymbol{J}_E^T)^\dagger \boldsymbol{J}_S^T(\boldsymbol{q}) \boldsymbol{f}_S \qquad (7)$$

where the Jacobian matrices $\boldsymbol{J}_E \in \mathbb{R}^{3\times 2}$ and $\boldsymbol{J}_S \in \mathbb{R}^{2\times 2}$ are

$$\boldsymbol{J}_S(\boldsymbol{q}) = \begin{bmatrix} L_{OS3} & 0 \\ 0 & L_{OS3} \end{bmatrix} \quad \boldsymbol{J}_E = \begin{bmatrix} L_E & 0 \\ 0 & L_E \\ 0 & 0 \end{bmatrix} \qquad (8)$$

with $L_{OS3} = L_S + L_R - q_3$ being the distance from point S to point O, L_R the distance from point R to point O when $q_3 = 0$, and L_E the shaft length. Both $\boldsymbol{f}_E$ and $\boldsymbol{f}_S$ are defined in the end-effector frame. Moreover, the third element of vector $\boldsymbol{f}_E$ computed in (7) is always null, because the trocar sensor allows to measure only the components of the interaction force lying

in the plane orthogonal to the instrument shaft, corresponding to the first two elements of $\boldsymbol{f}_E$.

B. Sensor Calibration

The calibration of the trocar sensor is aimed at computing the calibration matrix $\boldsymbol{W} \in \mathbb{R}^{2\times 2}$ in (6) which maps the vector of the sensed voltages $\boldsymbol{v}_S$ to the vector of the forces $\boldsymbol{f}_S$, i.e,

$$\boldsymbol{f}_S = \boldsymbol{W}\boldsymbol{v}_S.$$

We have chosen to directly compute the mapping between the external forces and the output voltages, and not that between the displacements δ_x and the forces, due to the simplicity to measure forces with respect to displacements. However, if matrix Q in (5) is known, the relationship between δ_x and voltages could also be obtained.

A commercial force-torque sensor ATI Mini 45 was attached to the instrument tip using a 3-D structure printed on purpose, with the axes of the ATI reference frame O_A-$x_A y_A z_A$ of the ATI sensor aligned to the axes of the end-effector frame. The calibration is performed by applying a force on the ATI sensor and reading the signals of the two sensors simultaneously. The ATI sensed forces are mapped to the trocar sensor frame using the equation

$$\boldsymbol{f}_A^S = \boldsymbol{J}_S^{-T}(\boldsymbol{q})\boldsymbol{J}_E^T\,\boldsymbol{f}_A \tag{9}$$

obtained by inverting the mapping (7). The numerical value of the calibration matrix was then derived as

$$\boldsymbol{W} = \boldsymbol{F}_A^S \boldsymbol{V}_S^{\dagger}$$

with $\boldsymbol{F}_A^S \in \mathbb{R}^{2\times n}$ and $\boldsymbol{V}_S \in \mathbb{R}^{2\times n}$ being the matrices obtained by stacking n samples of the measurements of $\boldsymbol{f}_A^S$ and $\boldsymbol{v}_S$, respectively.

We found experimentally that the trocar sensor exhibits different behaviors for positive and negative voltages. This is due to the nonperfect symmetry of the optical sensors that have been glued to the plastic frame. Hence, two different calibration matrices were identified

$$\boldsymbol{W}_P = \begin{bmatrix} 34.86 & -1.47 \\ -1.25 & 37.71 \end{bmatrix} \quad \boldsymbol{W}_N = \begin{bmatrix} 30.99 & -1.46 \\ -1.11 & 47.19 \end{bmatrix}$$

for positive and negative voltages, respectively. The following numerical values have been used: $L_S = 0.0254$ m, $L_R = 0.4046$ m, $L_E = 0.389$ m for a standard needle driver surgical instrument.

C. Sensor Characterization

The resolution of the trocar sensor depends on different factors. First of all, the output of the couple of optical sensors is an analog signal in the range ± 0.512 V that is converted to a digital signal by a 12-b ADC in differential configuration. Therefore, it is possible to define a voltage quantum $p = 0.512/2^{11}$ V, which is the minimal voltage value that can be discriminated.

Moreover, the resolution depends on the distance between the point where the external force is applied (the instrument tip) and the point where the sensitive element is placed. Such a distance is a function of the prismatic joint variable q_3. The effect on the force can be evaluated from the mapping (7) which allows to define the force resolution vector

$$\boldsymbol{\sigma} = (\boldsymbol{J}_E^T)^{\dagger}\,\boldsymbol{J}_S^T(\boldsymbol{q})\,\boldsymbol{W}\,\boldsymbol{p}$$

with $\boldsymbol{p} = [p,\, p]^T$. Hence, the resolution is not constant but depends on the prismatic joint position. In the following evaluation, without loss of generality, only the positive values matrix $\boldsymbol{W} = \boldsymbol{W}_P$ has been considered.

Therefore, the theoretical resolution of the sensing system in the range of motion $q_3 \in [70,\, 250]$ mm is $\boldsymbol{\sigma} = [0.0082,\, 0.0089]^T$ N in the worst case and $\boldsymbol{\sigma} = [0.0042,\, 0.0046]^T$ N in the best case. Without loss of generality, these quantities have been computed considering only the calibration matrix $\boldsymbol{W}_P$.

The measurement range of the sensor is also influenced by the value of the prismatic joint variable q_3. Considering that the sensor is designed to measure a force $\boldsymbol{f}_S$ in the range ± 20 N and assuming that q_3 is in the range $[70,\, 250]$ mm, from (7), it follows that the allowed range of $\boldsymbol{f}_E$ is between ± 10 N for $q_3 = 250$ mm and ± 19 N for $q_3 = 70$ mm.

D. Dynamic Modeling and Force Estimation

The forces measured by the sensor are influenced by gravity and inertial forces acting on the shaft. This means, for example, that the sensor measurements are different from zero even in the absence of interaction. Moreover, the sensor allows to measure only the components of the external force in the plane orthogonal to the axis of the shaft.

On the other hand, using a sensorless approach such as the residual-based technique [21], an estimation of the external force could be obtained from the currents and the dynamic model of the PSM moving the instrument. In this case, the estimation error will mainly depend on the accuracy of the dynamic model that should be carefully identified. An identification procedure for the dynamic parameters of the PSM arm of the dVRK robot is proposed in [29], where it is shown that an accurate identification is hard to obtain due to the relatively high measurement noise of the joint position sensors and the presence of nonnegligible dynamics effects, such as friction, elasticity, backlash, that are difficult to model. The experimental results presented in the next section show that the resolution that can be achieved using the residual-based approach alone is about 1 N, making this method unsuitable to measure small interaction forces.

The idea here is to improve the estimation of the external forces by combining the measurements obtained by the trocar sensor with the residual-based approach, which takes into account the dynamic interaction between the PSM arm and the sensor.

For this purpose, the dynamic model of the PSM arm and of the instrument can be computed by considering the kinematic chain composed by the actuated joint J_1, J_2, and J_3 of the PSM and the two passive joints J_4 and J_5 (see Fig. 5). The dynamic model can be computed using a Lagrangian approach, by taking the following into account:

1) the instrument can rotate with respect to the RCM about the axes J_1 and J_2, with joint variables q_1 and q_2, respectively;
2) the instrument can translate along the axis J_3, with joint variables q_3;

3) the instrument is modeled as a rigid cylinder which can rotate about the two passive revolute joints J_4 and J_5.

The equations of motion can be computed in terms of the vector of the generalized coordinates $\boldsymbol{\eta} = [\boldsymbol{q}^T,\ \boldsymbol{q}_S^T]^T$ as

$$\boldsymbol{B}(\boldsymbol{\eta})\ddot{\boldsymbol{\eta}} + \boldsymbol{C}(\boldsymbol{\eta},\dot{\boldsymbol{\eta}})\dot{\boldsymbol{\eta}} + \boldsymbol{g}(\boldsymbol{\eta}) + \boldsymbol{d}(\boldsymbol{\eta},\dot{\boldsymbol{\eta}}) = \boldsymbol{\tau}_M + \boldsymbol{J}^T(\boldsymbol{\eta})\boldsymbol{f}_E \tag{10}$$

where $\boldsymbol{B}(\boldsymbol{\eta}) \in \mathbb{R}^{5\times5}$ is the inertia matrix, $\boldsymbol{C}(\boldsymbol{\eta},\dot{\boldsymbol{\eta}}) \in \mathbb{R}^{5\times5}$, set so that $\dot{\boldsymbol{B}} = \boldsymbol{C} + \boldsymbol{C}^T$ is the Coriolis and centrifugal matrix, $\boldsymbol{g}(\boldsymbol{\eta}) \in \mathbb{R}^5$ is the gravity generalized torque, $\boldsymbol{d}(\boldsymbol{\eta},\dot{\boldsymbol{\eta}}) \in \mathbb{R}^5$ is the torque vector modeling viscous and Coulomb friction, the elasticity of the PSM cables, and other disturbances (see [29] for details). Moreover, $\boldsymbol{J}(\boldsymbol{\eta}) \in \mathbb{R}^{3\times5}$ is the Jacobian matrix, mapping the joint velocities to the translational velocity of the instrument tip referred to the end-effector frame and

$$\boldsymbol{\tau}_M = \begin{bmatrix}\boldsymbol{\tau}_R \\ \boldsymbol{\tau}_S\end{bmatrix} \tag{11}$$

where $\boldsymbol{\tau}_R \in \mathbb{R}^3$ is the vector of the motor torques acting on the first three joints of the PSM and $\boldsymbol{\tau}_S = \boldsymbol{J}_S^T(\boldsymbol{q})\boldsymbol{f}_S \in \mathbb{R}^2$ is the vector of the torques produced on the passive joints 4 and 5 by the force $\boldsymbol{f}_S$ sensed by the trocar sensor, being $\boldsymbol{J}_S(\boldsymbol{q})$, the Jacobian defined in (8).

The residual-based approach [21] allows to compute an estimate of the external force, assuming that the torque $\boldsymbol{\tau}_M$ and the dynamic model (10) of the system are known. The advantage of this approach is that the acceleration measurement, that is very noisy in most of the cases, is not needed.

In detail, the residual vector is defined as

$$\boldsymbol{r} = \boldsymbol{K}_I\left(\boldsymbol{B}(\boldsymbol{\eta})\dot{\boldsymbol{\eta}} - \int_0^t (\boldsymbol{r}(\sigma) + \boldsymbol{\tau}_M + \boldsymbol{n}(\boldsymbol{\eta},\dot{\boldsymbol{\eta}})\,d\sigma\right) \tag{12}$$

where

$$\boldsymbol{n}(\boldsymbol{\eta},\dot{\boldsymbol{\eta}}) = \boldsymbol{C}^T(\boldsymbol{\eta},\dot{\boldsymbol{\eta}})\dot{\boldsymbol{\eta}} - \boldsymbol{g}(\boldsymbol{\eta}) - \boldsymbol{d}(\boldsymbol{\eta},\dot{\boldsymbol{\eta}}) \tag{13}$$

and $\boldsymbol{K}_I \in \mathbb{R}^{5\times5}$ is a positive definite diagonal gain matrix.

The residual vector $\boldsymbol{r}$ satisfies the first-order equation

$$\dot{\boldsymbol{r}} = \boldsymbol{K}_I(\boldsymbol{\tau}_E - \boldsymbol{r}). \tag{14}$$

Hence, we can assume that

$$\boldsymbol{r} \simeq \boldsymbol{\tau}_E = \boldsymbol{J}^T(\boldsymbol{\eta})\boldsymbol{f}_E \tag{15}$$

although the convergence is asymptotic, depending on the choice of $\boldsymbol{K}_I$. Equation (15) corresponds to an overdetermined linear transformation that can be inverted to compute vector $\boldsymbol{f}_E$ from $\boldsymbol{r}$ using the weighted left inverse as

$$\boldsymbol{f}_E = (\boldsymbol{J}^T(\boldsymbol{\eta}))^{\dagger}\,\boldsymbol{r}. \tag{16}$$

This is a least squares solution, whose value depends on the choice of the weights of the left inverse matrix.

The computation of the components of the residual (12) requires the measurement of the vector of the generalized coordinates $\boldsymbol{\eta}$ (i.e., $\boldsymbol{q}$ and $\boldsymbol{q}_S$) and of its first time derivative $\dot{\boldsymbol{\eta}}$. While the measurements of the joint variables $\boldsymbol{q}$ of the PSM are available, and their time derivatives can be approximated via finite difference, the passive variables $\boldsymbol{q}_S$ and $\dot{\boldsymbol{q}}_S$ could be computed from the deflections of the trocar sensor. However, these deflections are very small and can be neglected in a first approximation. This produces a substantial simplification of the residual vector (12) and of the Jacobian $\boldsymbol{J}(\boldsymbol{\eta})$ that can be computed by setting $\boldsymbol{q}_S = \dot{\boldsymbol{q}}_S = \boldsymbol{0}$, and thus, $\boldsymbol{\eta} = [\boldsymbol{q}^T, \boldsymbol{0}^T]^T$ and $\dot{\boldsymbol{\eta}} = [\dot{\boldsymbol{q}}^T, \boldsymbol{0}^T]^T$. In particular, the Jacobian matrix can be computed as

$$\boldsymbol{J}^T(\boldsymbol{q}) = \begin{bmatrix} L_{OE3}c_2 & 0 & 0 \\ 0 & L_{OE3} & 0 \\ 0 & 0 & 1 \\ L_E & 0 & 0 \\ 0 & L_E & 0 \end{bmatrix} \tag{17}$$

with $c_i = \cos(q_i)$, $s_i = \sin(q_i)$, and $L_{OE3} = L_R - L_E - q_3$.

By inspecting the Jacobian matrix in (17) and in view of (15), it is possible to see that the external force along the x_E and y_E axes of the end-effector frame can be estimated by considering either the first two residual values ($\boldsymbol{r}_{12}$) or the last two ($\boldsymbol{r}_{45}$). Therefore, the vector $\boldsymbol{f}_E$ of the external forces can be computed in the following three different ways:

A) from the first three components of the residual vector $\boldsymbol{r}$ in (12) which, in view of (11), depend only on the motor torques $\boldsymbol{\tau}_R$, without making use of the measured force $\boldsymbol{f}_S$;

B) from the last three components of the residual vector $\boldsymbol{r}$ in (12); namely, r_3, which depends on the motor torque of the prismatic joint J_3, allows to estimate f_{zE}, while $\boldsymbol{r}_{45}$, which depends on the measured force $\boldsymbol{f}_S$, allows to estimate f_{xE} and f_{yE};

C) from (16), with suitable weights in the left inverse; the criterion to adopt for the weights selection should be that of using the force sensor information when the force is in the trocar sensor measurement range, and the motor currents when outside this range.

In this article, to gain a better insight into the accuracy of the different available input data (motor currents and force sensor readings) the cases A) and B) are considered.

In particular, in case A), the first three components of the residual vector (12) depend on the base parameters of PSM arm and instrument, by considering only the first three joints and assuming that the instrument is rigidly connected to the arm. The symbolic expressions of these parameters and their identified numerical values can be found in [29].

In case B), the last three components of the residual vector (12) can be computed in terms of a reduced subset of dynamic parameters of the PSM and of the instrument shaft. In detail, in view of (15) and (17), vector $\boldsymbol{f}_E$ can be computed as

$$\boldsymbol{f}_E = \begin{bmatrix} r_4/L_E \\ r_5/L_E \\ r_3 \end{bmatrix}. \tag{18}$$

The vector $\boldsymbol{r}_{45}$ collecting the last two components of the residual vector (12) can be expressed as

$$\boldsymbol{r}_{45} = \boldsymbol{K}_{45I}\left(\boldsymbol{B}_{xy}(\boldsymbol{q})\dot{\boldsymbol{q}} - \int_0^t (\boldsymbol{r}_{45}(\sigma) + \boldsymbol{\tau}_S + \boldsymbol{n}_{xy}(\boldsymbol{q},\dot{\boldsymbol{q}}))\,,d\sigma\right)$$

TABLE I
CAD DYNAMIC PARAMETERS OF THE INSTRUMENT SHAFT

parameter	value	parameter	value
mp_{xS}	$-5.1e^{-3}$	I_{yyS}	$8e^{-4}$
I_{xxS}	$2.8e^{-7}$	I_{zzS}	$8e^{-4}$

with

$$\boldsymbol{B}_{xy}(\boldsymbol{q}) = \begin{bmatrix} b_{x1} & 0 \\ 0 & b_{y2} \end{bmatrix}$$

$$\boldsymbol{n}_{xy}(\boldsymbol{q}, \dot{\boldsymbol{q}}) = \begin{bmatrix} c_{x1}\dot{q}_1 + c_{x2}\dot{q}_2 + c_{x3}\dot{q}_3 - g_x \\ c_{y1}\dot{q}_1 + c_{y3}\dot{q}_3 - g_y \end{bmatrix}$$

and

$$\begin{aligned}
b_{x1} &= (mp_{xS}(q_3 - L_R) - I_{yyS})\, c_2 \\
b_{y2} &= mp_{xS}(q_3 - L_R) - I_{zzS} \\
c_{x1} &= (I_{xxS} + I_{yyS} - I_{zzS}) s_2 \dot{q}_2 \\
c_{x2} &= -(I_{yyS} - I_{xxS} + I_{zzS} + mp_{xS}(L_R - 2q_3))\, s_2 \dot{q}_1 \\
c_{x3} &= -2mp_{xS} c_2 \dot{q}_1 \\
c_{y1} &= -2\,(I_{xxS} - I_{yyS} + (2q_3 - L_R)mp_{xS})\, s_2 c_2 \dot{q}_1 \\
c_{y3} &= -2mp_{xS}\dot{q}_2 \\
g_x &= 9.81\, mp_{xS} c_1 s_2 \\
g_y &= 9.81\, mp_{xS} s_1.
\end{aligned}$$

In the abovementioned equations, mp_{xS} is a first moment of the instrument shaft, and I_{xxS}, I_{yyS}, I_{zzS} are the elements of its inertia matrix. The numerical values of these parameters, for a standard da Vinci needle driver instrument, were derived using CAD and are reported in Table I. The quantities are referred to frame O_5-$x_5y_5z_5$ of Fig. 5 and expressed in SI basic standard measurement units that are omitted here for brevity.

The third component of the residual vector (12) can be expressed in the form

$$r_3 = k_{3I}\left(\boldsymbol{b}_z^T(\boldsymbol{q})\dot{\boldsymbol{q}} - \int_0^t (r_3(\sigma) + \tau_{3R} + n_z(\boldsymbol{q}, \dot{\boldsymbol{q}}))\, d\sigma\right)$$

with

$$\boldsymbol{b}_z^T(\boldsymbol{q}) = [b_{z1} \quad b_{z2} \quad b_{z3}]$$

$$n_z(\boldsymbol{q}, \dot{\boldsymbol{q}}) = c_{z1}\dot{q}_1 + c_{z2}\dot{q}_2 - g_z - f_z$$

and

$$\begin{aligned}
b_{z1} &= mp_{yI} c_2 \\
b_{z2} &= mp_{xI} \\
b_{z3} &= m_I + m_C \\
c_{z1} &= 2mp_{yI} s_2 \dot{q}_2 - 0.0312 m_I c_2^2 \dot{q}_1 + 0.4 m_C c_2^2 \dot{q}_1 \\
&\quad + 2mp_{zI} c_2^2 \dot{q}_1 + 2(m_I + m_C) q_3 c_2^2 \dot{q}_1 + 2mp_{xI} c_2 s_2 \dot{q}_1 \\
c_{z2} &= 0.4 m_C \dot{q}_2 - 0.0312 m_I \dot{q}_2 - 2mp_{zI}\dot{q}_2 \\
&\quad + 2(m_I + m_C) q_3 \dot{q}_2
\end{aligned}$$

TABLE II
IDENTIFIED DYNAMIC PARAMETERS OF THE PSM

parameter	value	parameter	value
m_I	0.146	m_C	0.179
mp_{xI}	0.001	F_{vI}	2.695
mp_{yI}	0.033	F_{sI}	0.496
mp_{zI}	-0.039		

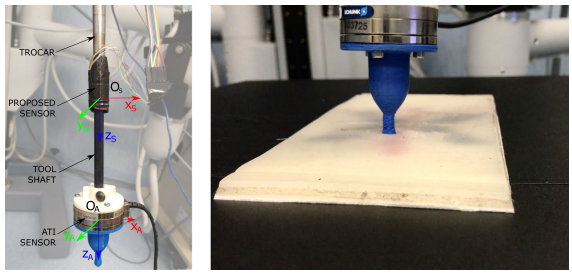

(a) (b)

Fig. 7. Experimental setup. (a) ATI Mini 45 force sensor mounted at the end-tip of the surgical instrument; the two reference frames are, respectively, that of the force sensor in the trocar (top) and that of the ATI sensor (bottom) and (b) Interaction of the spherical probe attached at the bottom of the ATI sensor with a soft tissue phantom.

$$\begin{aligned}
g_z &= -9.81(m_I - m_C) c_1 c_2 \\
f_z &= F_{vI}\dot{q}_3 + F_{sI}\tanh(50\,\dot{q}_3).
\end{aligned}$$

In the abovementioned equations, m_I is the mass of the translating link of the PSM, mp_{xI}, mp_{yI}, mp_{zI} are the corresponding first moments, m_C is the mass of the counterweight, and F_{vI}, F_{sI} are friction coefficients. The numerical values of the abovementioned parameters, for the experimental setup used in this article, have been estimated through the identification procedure presented in [29] and are reported in Table II. The quantities are referred to frame O_E-$x_Ey_Ez_E$ and are expressed in SI basic standard measurement units that are omitted here for brevity.

IV. EXPERIMENTAL VALIDATION

This section is devoted to the experimental validation of the sensor in static and dynamic conditions, by using an ATI Mini 45 force sensor, mounted at the end-tip of the surgical instrument, as ground truth.

A. Static Validation

To cancel the effects of gravity, a force is applied to the ATI sensor while keeping the shaft of the surgical instrument aligned to the vertical direction, as shown in Fig. 7(a). A motion of the instrument along the vertical direction is commanded, by considering a constant velocity displacement of 0.1 m of the prismatic joint q_3, in order to test the trocar sensor for different distances of the instrument tip from the position of the sensitive elements. Fig. 8 reports the time histories of the components along the axes x_E and y_E of the force measured by the ATI sensor and of the force estimated by using the trocar sensor and (7).

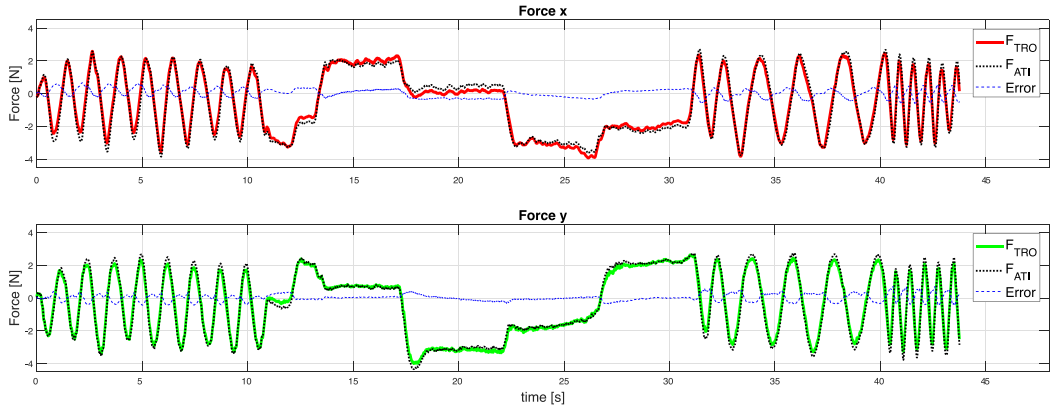

Fig. 8. Static characterization. Force along the axis x_E (top), force along the axis y_E (bottom).

The results show that the trocar sensor has a good response, close to that of the commercial sensor ATI mini 45. The relative error between the force components measured by the ATI sensor and the trocar sensor is less than 12% along both the axes. The error is higher in the central region of the graph, when a constant force is applied. This is due to the undesired hysteresis effects of the material used for the prototype.

B. Dynamic Validation

The validation of the complete dynamic model has been performed on a simulated diagnostic procedure involving the interaction between the instrument and a soft tissue phantom.

A spherical probe was attached at the bottom of the ATI sensor mounted at the end-tip of the instrument shaft [see Fig. 7(b)]. By using the PSM arm in telemanipulation mode, the probe was pushed against the soft tissue phantom. The dynamic parameters reported in Tables I and II have been properly updated to take into account the mass and inertia of the ATI sensor.

The estimation of the external force was performed considering both methods A) and B) described in Section III-D. The time histories of the estimated force components together with the corresponding quantities measured using the ATI force sensor are shown in Fig. 9. In the first three plots, the force components along the axes x_E, y_E, and z_E computed with method A) are reported. The last two plots show the components along the axes x_E and y_E computed with method B), using the trocar sensor measurements. The visual inspection of the plots shows that the trocar sensor allows a more accurate estimation of the force components along the directions x_E and y_E, compared to those computed with method A).

A quantitative analysis, in terms of the RMS errors reported in Table III, shows that with method B), the errors are one-tenth lower than with method A).

From the experimental data, it is possible to observe that, for the considered setup, the resolution of the force estimation using method A) is of about 1 , which decreases to 0.1 N for the components in the plane orthogonal to the instrument shaft axis estimated with method B) using the trocar sensor. It is worth pointing out that this value is larger than the theoretical resolution that could be obtained with the trocar sensor in ideal conditions and in the absence of motion.

V. Vision-Based Force Feedback

The estimation of the two components of the external force provided by the trocar sensor is used here to develop an intuitive force feedback method based on augmented reality.

In our surgical system, frame grabbers capture real-time stereoscopic images from the dVRK InSite stereo endoscope. The force is visualized on the two rectified stereo images with a graphic overlay following the instrument motion. To guarantee the intuitiveness of the proposed approach, the overlay is defined in the end-effector frame $O_E - x_E y_E z_E$ and follows the tool during the motion, as reported in the screenshots of Fig. 10.

The intuitiveness with respect to the lack of the measurement of the force along the axis z_E is preserved by representing the vector composed by the first two force components (f_{xE} and f_{yE}) directly in the plane orthogonal to the instrument axis. Moreover, the force vector is visualized with a directed line segment (i.e., a geometric vector) with initial point on the tool's tip, then it is always inside the field of view. The graphical overlay is updated on the surgeon's stereoscopic display console with a frequency of 30 frames per second. The geometric vector can change length, direction, and color to visualize the following three different kinds of information.

1) Force amplitude in a range $[0, f_{\max}]$ proportional to the vector length.
2) Force direction on the plane orthogonal to the instrument axis through the vector direction.
3) Force thresholds set for particular surgical phases codified through the vector color.

To be more precise, the geometric vector connects the origin O_E of the end-effector frame to point P_T, whose position vector $\boldsymbol{p}_T$, expressed in the base frame, is computed as

$$\boldsymbol{p}_T = \boldsymbol{o}_E + \boldsymbol{R}_E \boldsymbol{l}$$

with $\boldsymbol{o}_E$ being the position vector of O_E and $\boldsymbol{R}_E$ the rotation matrix of the end-effector frame with respect to the robot base

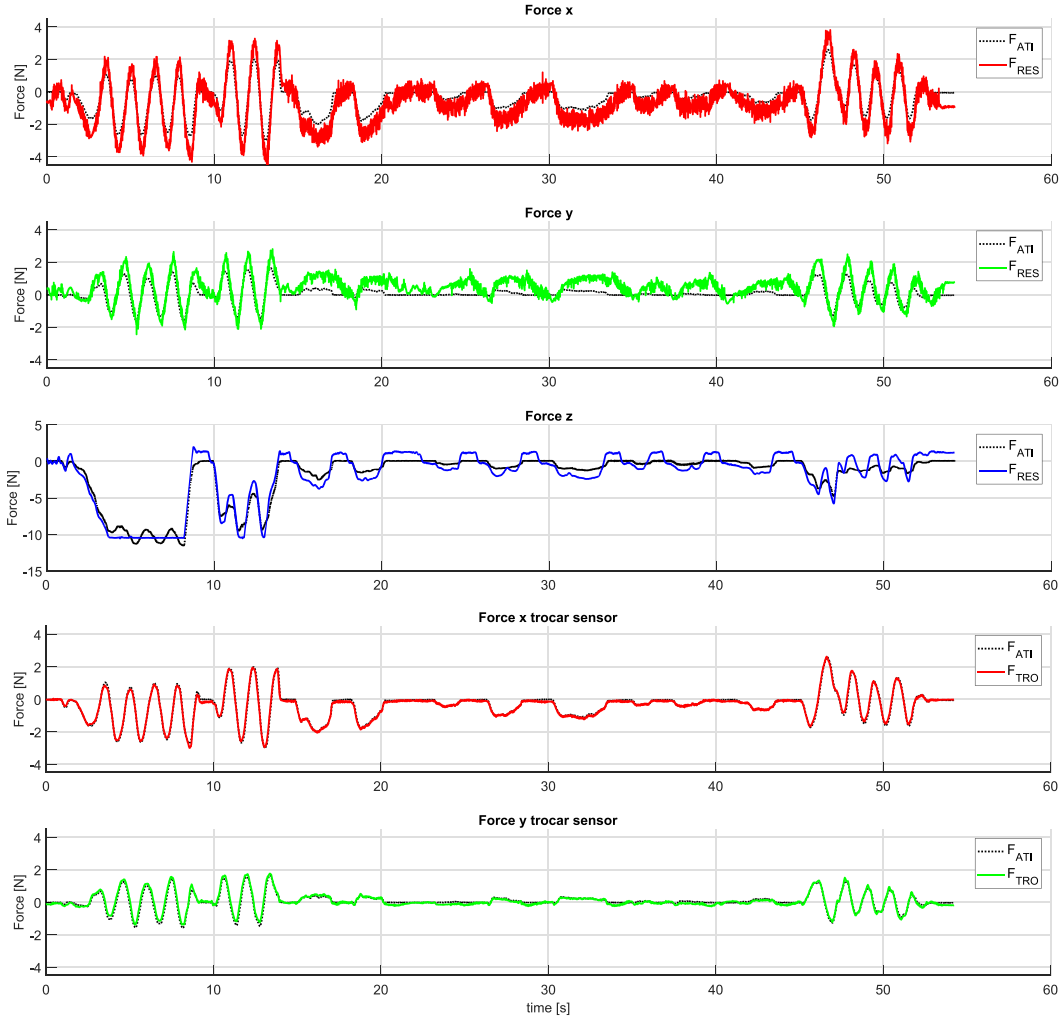

Fig. 9. Time histories of the estimated force. Method A) is used in the first three plots from the top and method B) in the last two plots.

frame. These quantities are computed from the joint vector $\boldsymbol{q}$ using the PSM direct kinematics. Moreover, vector $\boldsymbol{l}$ is defined as $\boldsymbol{l} = l_{\max}/f_{\max}\boldsymbol{f}_E$ with $l_{\max}$ being the length of the geometric vector when $\|\boldsymbol{f}_E\| = f_{\max}$. Points P_T and O_E are projected on the rectified stereo image plane considering the known pinhole camera model transformation and the hand–eye calibration matrices between the camera left/right frames and the robot base frame, obtained using the method proposed in [30]. Finally, the vector color is set according to a continuous gradient scale between the green and the red color defined by the following RGB code:

$$\boldsymbol{c} = [\alpha|\boldsymbol{f}_E|/f_{\max}, \quad \alpha(1 - |\boldsymbol{f}_E|/f_{\max}), \quad 0]$$

with $\alpha = 255$.

In our framework, the task-related force thresholds are set empirically based on the average force the surgeon exerts while performing the specific task. In the experiment presented in this article, the following parameters are used: $f_{\max} = 5$ N; $l_{\max} = 0.02$ m; green color for force less than 2 N; yellow color for force in the range $[2 - 4]$ N; red color for force up to 5 N. Three typical surgical subtasks have been considered—tissue palpating, needle passing, knot tying. The results are shown in Fig. 10, reporting the variation in direction, length, and color of the overlapped geometric vectors. A video showing the sensing device and the proposed experiment can be downloaded[2].

TABLE III
RMS ERRORS USING METHODS A) AND B)

method	$RMSe_x$[N]	$RMSe_y$[N]	$RMSe_z$[N]
(A)	0.618	0.9027	0.949
(B)	0.094	0.112	0.949

VI. DISCUSSION

In this section, a number of issues related to the proposed trocar sensor is discussed. First of all, as it happens for many commercial sensors, our solution requires an offset calibration every time the sensor is switched ON. However, for the trocar sensor, a new calibration is also needed anytime the surgical

[2][Online]. Available: https://youtu.be/YxIBzTMlKFo.

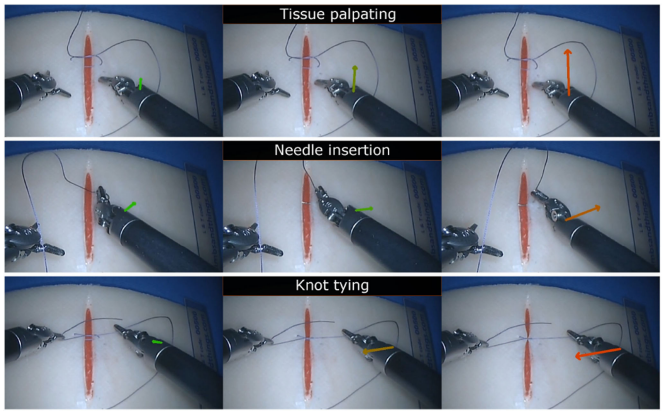

Fig. 10. Vision-based force feedback. The tissue reaction force is shown in augmented reality. Top: Tissue pushing, Middle: Needle insertion, Bottom: Knot tying.

instrument is replaced. This is due to the possible geometric differences between instruments, which may not be perfectly aligned with the trocar. Moreover, to make the calibration independent from the joint configuration of the robot arm, the instrument-dependent gravity torques must be suitably compensated before the calibration starts.

The instrument physical properties (length, mass, inertia) should be taken into account in the sensor static and dynamic model; however, for standard lightweight instruments, the dynamic effects are usually small compared to the range of the measured forces and can also be neglected.

Finally, the prototype tested in the article was developed using a PolyJet printing technology only as a proof of concept. The development of a prototype suitable to be used in a real surgical scenario is in our future plans. The material for the new sensor will be chosen so as to be biocompatible, to have good response to stresses without hysteresis, and suited to sterilization. Moreover, suitable seals will be designed to prevent the penetration of body fluids inside the sensor.

VII. Conclusion

In this article, a new concept of force sensing for MIRS was proposed and evaluated. The presented solution differs from the MIRS force sensors presented in the literature since it does not require the modification of the surgical instruments, the force sensor being placed in the trocar. This opens the way for new disposable, low-cost force sensors that can be tool independent, allowing the use of force feedback on different robotic surgical systems. As an example of possible use of the force measured by the trocar sensor, a simple and intuitive vision-based force feedback solution was tested on a da Vinci surgical robot. In future works, the method C) described in Section III will be implemented to extend the measurement range outside the trocar sensor range.

References

[1] G. A. Fontanelli, L. Buonocore, F. Ficuciello, L. Villani, and B. Siciliano, "A novel force sensing integrated into the trocar for minimally invasive robotic surgery," in *Proc. IEEE/RSJ Int. Conf. Intell. Robots Syst.*, 2017, pp. 131–136.

[2] T. Ortmaier, B. Deml, G. Passig, D. Reintsema, and U. Seibold, "Robot assisted force feedback surgery," *Adv. Telerobot.*, vol. 31, pp. 361–379, 2007.

[3] M. Selvaggio, G. A. Fontanelli, F. Ficuciello, L. Villani, and B. Siciliano, "Passive virtual fixtures adaptation in minimally invasive robotic surgery," *IEEE Robot. Autom. Lett.*, vol. 3, no. 4, pp. 3129–3136, Oct. 2018.

[4] N. Zemiti, G. Morel, T. Ortmaier, and N. Bonnet, "Mechatronic design of a new robot for force control in minimally invasive surgery," *IEEE/ASME Trans. Mechatronics*, vol. 12, no. 2, pp. 143–153, Apr. 2007.

[5] U. Kim, D. H. Lee, Y. B. Kim, D. Y. Seok, J. So, and H. R. Choi, "S-surge: Novel portable surgical robot with multiaxis force-sensing capability for minimally invasive surgery," *IEEE/ASME Trans. Mechatronics*, vol. 22, no. 4, pp. 1717–1727, Aug. 2017.

[6] A. Petit, F. Ficuciello, G. A. Fontanelli, L. Villani, and B. Siciliano, "Using physical modeling and RGB-D registration for contact force sensing on deformable objects," in *Proc. IEEE Int. Conf. Inform. Control, Autom. Robot.*, 2017, pp. 24–33.

[7] F. Ficuciello, L. Villani, and B. Siciliano, "Variable impedance control of redundant manipulators for intuitive human– robot physical interaction," *IEEE Trans. Robot.*, vol. 31, no. 4, pp. 850–863, Aug. 2015.

[8] F. Ficuciello, L. Villani, and B. Siciliano, "Impedance control of redundant manipulators for safe human-robot collaboration," *Acta Polytech. Hung.*, vol. 13, pp. 223–238, 2016.

[9] R. J. Brooks, T. Looi, G. Azzie, J. Drake, and J. T. Gerstle, "Force-sensing sleeve for laparoscopic surgery," *J. Med. Devices*, vol. 10, pp. 1–2, 2016.

[10] R. Haslinger, P. Leyendecker, and U. Seibold, "A fiberoptic force-torque-sensor for minimally invasive robotic surgery," in *Proc. IEEE Int. Conf. Robot. Autom.*, 2013, pp. 4390–4395.

[11] M. C. Yip, S. G. Yuen, and R. D. Howe, "A robust uniaxial force sensor for minimally invasive surgery," *IEEE Trans. Biomed. Eng.*, vol. 57, no. 5, pp. 1008–1011, May 2010.

[12] P. Puangmali, H. Liu, L. D. Seneviratne, P. Dasgupta, and K. Althoefer, "Miniature 3-axis distal force sensor for minimally invasive surgical palpation," *IEEE/ASME Trans. Mechatronics*, vol. 17, no. 4, pp. 646–656, Aug. 2012.

[13] P. Polygerinos, L. D. Seneviratne, R. Razavi, T. Schaeffter, and K. Althoefer, "Triaxial catheter-tip force sensor for MRI-guided cardiac procedures," *IEEE/ASME Trans. Mechatronics*, vol. 18, no. 1, pp. 386–396, Feb. 2013.

[14] A. Cirillo, F. Ficuciello, C. Natale, S. Pirozzi, L. Villani, and B. Siciliano, "A conformable force/tactile skin for physical human– robot interaction," *IEEE Robot. Autom. Lett.*, vol. 1, no. 1, pp. 41–48, Jan. 2016.

[15] L. Viry *et al.*, "Flexible three-axial force sensor for soft and highly sensitive artificial touch," *Adv. Mater.*, vol. 26, pp. 2659–2664, 2014.

[16] Q. Liang, D. Zhang, G. Coppola, Y. Wang, S. Wei, and Y. Ge, "Multi-dimensional MEMS/micro sensor for force and moment sensing: A review," *IEEE Sensors J.*, vol. 14, no. 8, pp. 2643–2657, Aug. 2014.

[17] M. O. Culjat *et al.*, "A tactile feedback system for robotic surgery," in *Proc. IEEE Int. Conf. Eng. Med. Biol. Soc.*, 2008, pp. 1930–1934.

[18] O. H. Paydar *et al.*, "Fabrication of a thin-film capacitive force sensor array for tactile feedback in robotic surgery," in *Proc. IEEE Int. Conf. Eng. Med. Biol. Soc.*, 2012, pp. 2355–2358.

[19] D. H. Lee, U. Kim, T. Gulrez, W. J. Yoon, B. Hannaford, and H. R. Choi, "A laparoscopic grasping tool with force sensing capability," *IEEE/ASME Trans. Mechatronics*, vol. 21, no. 1, pp. 130–141, Feb. 2016.

[20] G. A. Fontanelli, M. Selvaggio, L. R. Buonocore, F. Ficuciello, L. Villani, and B. Siciliano, "A new laparoscopic tool with in-hand rolling capabilities for needle reorientation," *IEEE Robot. Autom. Lett.*, vol. 3, no. 3, pp. 2354–2361, Jul. 2018.

[21] A. de Luca and R. Mattone, "Sensorless robot collision detection and hybrid force/motion control," in *Proc. IEEE Int. Conf. Robot. Autom.*, 2005, pp. 999–1004.

[22] S. Shimachi, S. Hirunyanitiwatna, Y. Fujiwara, A. Hashimoto, and Y. Hakozaki, "Adapter for contact force sensing of the da Vinci robot," *Int. J. Med. Robot. Comput. Assisted Surg.*, vol. 4, pp. 121–130, 2008.

[23] P. Kazanzidesf, Z. Chen, A. Deguet, G. S. Fischer, R. H. Taylor, and S. P. Dimaio, "An open-source research kit for the da Vinci surgical system," in *Proc. IEEE Int. Conf. Robot. Autom.*, 2014, pp. 6434–6439.

[24] A. M. Okamura, "Haptic feedback in robot-assisted minimally invasive surgery," *Curr. Opin. Urol.*, vol. 19, pp. 102–107, 2009.

[25] D. Prattichizzo, C. Pacchierotti, and G. Rosati, "Cutaneous force feedback as a sensory subtraction technique in haptics," *IEEE Trans. Haptics*, vol. 5, no. 4, pp. 289–300, Oct./Dec. 2012.

[26] A. Talasaz, A. L. Trejos, and R. V. Patel, "The role of direct and visual force feedback in suturing using a 7-DOF dual-arm teleoperated system," *IEEE Trans. Haptics*, vol. 10, no. 2, pp. 276–287, Apr./Jun. 2017.

[27] R. C. Jackson and M. C. Cavusoglu, "Modeling of needle-tissue interaction forces during surgical suturing," in *Proc. IEEE Int. Conf. Robot. Autom.*, 2012, pp. 4675–4680.
[28] H. K. H. Kang and J. Wen, "Robotic knot tying in minimally invasive surgeries," in *Proc. IEEE/RSJ Int. Conf. Intell. Robots Syst.*, 2002, pp. 1421–1426.
[29] G. A. Fontanelli, F. Ficuciello, L. Villani, and B. Siciliano, "Modelling and identification of the da Vinci research kit robotic arms," in *Proc. IEEE/RSJ Int. Conf. Intell. Robots Syst.*, 2017, pp. 1464–1469.
[30] Z. Zhang, L. Zhang, and G. Z. Yang, "A computationally efficient method for hand–eye calibration," *Int. J. Comput. Assisted Radiol. Surg.*, vol. 12, pp. 1775–1787, 2017.

Giuseppe Andrea Fontanelli received the Ph.D. degree in computer and automation engineering from the University of Naples Federico II, Napoli, Italy, in 2018.

He is currently a Postdoctoral Researcher with the Department of Electrical Engineering and Information Technology, University of Naples Federico II. His research interests include mechatronic design, tele-manipulation, shared control, and robotic surgery, with particular interest in mechatronic design of sensors, tools, and advanced shared control strategies for sensory motor enhancement in surgical scenarios.

Luca Rosario Buonocore received the Ph.D. degree in computer and automation engineering from the University of Naples Federico II, Napoli, Italy, in 2015.

He is currently a Research Fellow with the R&D Robotic Division, Engineering Group, CERN, Meyrin, Switzerland. His main research interests include mechatronic design of novel robotic solutions, such as mobile robotic platforms and ultralight robotic arms for areal manipulation.

Fanny Ficuciello (Senior Member, IEEE) received the Ph.D. degree in computer and automation engineering from the University of Naples Federico II, Napoli, Italy, in 2010.

She is currently an Assistant Professor with the Department of Electrical Engineering and Information Technology, University of Naples Federico II. Her research interests include biomechanical design and control strategies for anthropomorphic artificial hands, grasping and manipulation with dual hand/arm robotic systems, human–robot interaction control, and surgical robotics.

Luigi Villani (Senior Member, IEEE) received the Research Doctorate degree in electrical engineering and computer science from the University of Naples Federico II, Napoli, Italy, in 1996.

He is currently a Full Professor of Automatic Control with the University of Naples Federico II. His research interests include force/motion control of manipulators, safe physical human–robot interaction, cooperative robot manipulation, human–robot interaction, visual servoing, industrial and service robotics, and surgical robotics.

Bruno Siciliano (Fellow, IEEE) received the Research Doctorate degree in electronic engineering from the University of Naples Federico II, Napoli, Italy, in 1987.

He is currently a Full Professor of Robotics with the University of Naples Federico II. He is the Director of the Interdepartmental Center for Advanced Robotics in Surgery and responsible for the PRISMA Lab, University of Naples Federico II. His research interests include force and visual control, lightweight flexible arms, human–robot interaction, aerial and service robotics, and surgical robotics.